Alma Mater Studiorum Università di Bologna
Archivio istituzionale della ricerca

A Novel 3-D Printed Dual-Port Rectenna for Simultaneous Energy Harvesting and Backscattering of a Passively Generated UWB Pulse

(Article begins on next page)

11 July 2024

A Novel 3-D Printed Dual-Port Rectenna for Simultaneous Energy Harvesting and Backscattering of a Passively Generated UWB Pulse

Giulia Battistini, *Student Member, IEEE*, Giacomo Paolini, *Member, IEEE*, Alessandra Costanzo, *Fellow, IEEE*, and Diego Masotti, *Senior Member, IEEE*

Abstract—**This work presents the design and characterization of a new compact rectenna system, fully 3-D printed on a low-cost material, the polylactic acid (PLA). The rectenna consists of a patch-like antenna, with two orthogonal excitation ports, suitably designed to achieve both ultra-high frequency (UHF) and ultra-wideband (UWB) cross-polarized radiation performance. The first port harvests multi-tone RF power at UHF, around 2.47 GHz (for the present case 8 equally spaced non-synchronized tones are used); the second port backscatters the intermodulation products generated by the rectifier, realizing a quasi-UWB pulse. The rectifier consists of a single-diode embedded into two linear subnetworks: one, connecting the UHF port and the diode, is co-designed to ensure DC-block and rectifier-antenna matching in the UHF band; the second one combines a high-pass filter, connecting the diode and the UWB port, to backscatter the passive pulse, and a DC path to collect the converted DC power. The 3-D etching of the low-cost substrate is optimized to obtain antenna performance comparable to those achieved with specialized RF materials. The system design is carried out by integrating full-wave and nonlinear simulations with the manifold goal of minimizing the overall footprint, ensuring UWB-mask-compatible radiated spectra and RF-to-DC conversion efficiency. A 3-D printed prototype has been realized and experimentally characterized. With a total received power of –15 dBm, equally distributed over 8 tones spaced by 1 MHz, a quasi-UWB pulse power peak of about 80 nW has been demonstrated.**

Index Terms—**3-D printing, backscattering, energy harvesting, localization, UWB.**

Fig. 1. (a) Schematic overview of the proposed 3-D printed rectenna with augmented functionalities: at the ultra-high frequency (UHF) port a multi-sine RF power is received; the nonlinear rectifier converts it into DC and into higher harmonic intermodulation products that are radiated through the ultra-wideband (UWB) port; (b) block diagram of the system integrated with low-power control electronics for energy-autonomous UWB communication and sensing.

I. INTRODUCTION

IN the last years, the additive manufacturing (AM) process has allowed three-dimensional (3-D) printing to become a powerful tool for the engineering of the electromagnetic

(EM) properties of materials and structures [1].

The traditional subtracting methods, such as micromachining and etching, have led to the creation of fancy and complex bi-dimensional layouts [2], [3], but with no access to the internal part of the structure. 3-D printing bridges this gap, by a fast and inexpensive fabrication process which allows to tailor the dielectric characteristics [relative permittivity (ε_r) and conductivity (σ)]. This is obtained in 3-D, by regulating the material infill percentage and the empty/full pattern ratio. In this way the designer takes advantage of an almost unlimited number of degrees of freedom in the material synthesis, even in the microwave/millimeter-wave range for both circuit [4] and antenna [5] applications. 3-D printing is particularly suitable to meet the internet of things (IoT) requirements in terms of miniaturized, low-cost electronic technologies for healthcare applications, where wearable, lightweight, non-invasive systems need to be adapted to curvilinear surfaces of the body [6]. Furthermore, the engineered material can be co-designed with respect to its mechanical properties that can be varied with the application, i.e., by deploying a low infill percentage with a high empty/full ratio if efficiency is the primary goal (as for radiative applications [1]), and a high infill percentage for miniaturization purposes.

Fig. 1(a) shows the system overview of the 3-D printed rectenna (rectifying antenna) proposed in this work, where the radiative and circuital sub-systems are realized on a thick (2 mm) and high empty/full ratio material and on a thin (0.5 mm) full substrate, respectively, in a seamless way. Such system provides at the same time energy autonomy [7]–[9] and high-accuracy localization capabilities [10] exploiting a passively generated quasi-UWB pulse. Indeed, localization using impulse-radio ultra-wideband (IR-UWB) technique has already demonstrated sub-meter accuracy and robustness to interference [11]–[13].

The system of Fig. 1(a) satisfies all these constraints by using the 3-D printable, cheap, and lossy material polylactic acid (PLA) for the AM process. A preliminary system architecture has been presented in [14] and has been derived from structures available in the literature mimicking those of living organisms, such as honeycombs, to provide low weight and excellent damage resistance abilities [4], [15]–[18].

The present work proposes for the first time a non-planar structure of the 3-D printed PLA whose core etching, and thus the empty/fill ratio, is carried out accounting for the operating frequency and the radiation and circuital performance, as detailed in Section II. Then, the engineered 3-D structure is adopted to co-design a novel advanced microwave system which is able to simultaneously perform energy harvesting (EH) activity, e.g., for supplying a low-power microcontroller unit (MCU) and/or sensor, and to generate a quasi-UWB signal for indoor localization, using a novel two-port antenna structure.

Several two-port rectennas operating at both single-frequency [19] and multi-band [20] have been presented for narrow-band simultaneous wireless information and power transfer (SWIPT) [21]. In [22], a combined UHF-UWB antenna is presented but it is not suitable for wearable applications because of its ungrounded nature and UHF and UWB are not cross-polarized.

For this purpose, a novel dual-port patch-like antenna is designed on the 3-D printed material for the reception of a multi-sine UHF signal for EH [23] and the backscattering of a quasi-UWB signal, generated by harvesting the intermodulation (IM) products of the multi-sine excitation [24].

The solution proposed in this work, thanks to the adopted thick 3-D-printed substrate with a background plane, allows to exploit UWB radiation on body with high decoupling from it, as required by wearable systems as the one addressed in this work. To the authors' knowledge, a dual-port wearable antenna covering cross-polarized UHF and UWB bands is presented in this work for the first time.

The whole nonlinear rectifying and backscattering system is designed by resorting to an effective combination of circuital and full-wave simulations, where all the IM products falling in the UWB band are considered without affecting the central processing unit (CPU) simulation time [24]. Finally, the measurement campaign of the realized prototype provides the demonstration of the productive usage of the engineered PLA for the creation of a compact system able to autonomously generate strong enough quasi-UWB signals for localization purposes. Fig. 1(b) shows the block diagram of an extended system consisting of the proposed dual-mode rectenna integrated with low-power control electronics, powered by the harvested energy, to support energy-autonomous UWB communication and sensing.

The paper is organized as follows: Section II offers a detailed description of the 3-D printed substrate hosting the antenna part and demonstrates the effectiveness of the adopted optimized structure for the design of the novel two-port antenna; Section III is devoted to the co-design (circuital and full-wave) of the dual-port system acting both as a rectenna in the UHF band and as a passive backscattering tag in the UWB band. Finally, Section IV shows the experimental demonstration of both the EH and the UWB signal generation and the radiation performance of the whole system.

II. MATERIAL CHARACTERIZATION AND ENGINEERING

Usually, materials for AM are selected for properties such as elasticity, waterproof, mechanical robustness or temperature resistance and lack from satisfying the requirements for EM applications: by 3-D etching, they can be worked out to fill this gap. Therefore, it is necessary to accurately derive the dielectric properties of test-printed samples before starting the RF design based on these non-conventional substrates. The Ultimaker 3 Extended 3-D printer (minimum layer thickness: 20 μm, XY accuracy: 12.5 μm) is used. Printer settings, such as resolution, speed, and infill factor, are fundamental for creating high-accuracy prototypes in terms of well-defined dielectric properties, permittivity ε_r and loss tangent $tan\delta$. An uncertainty margin in the accuracy of the samples printed by fused deposition molding (FDM) must be accounted for, due to material shrinkage during the cooling down phase or uncontrolled material flow which generates small air gaps

(a)   (b)

Fig. 2. Photographs of the fabricated T-resonators with adhesive copper on (a) 0.5 mm and (b) 2-mm-thick PLA samples.

TABLE I
PLA EM CHARACTERIZATION RESULTS

Freq. (GHz)	ε'		ε''		$tan\delta$	
	0.5 mm	2 mm	0.5 mm	2 mm	0.5 mm	2 mm
2	2.65	2.64	0.05	0.05	0.019	0.019
5	2.64	2.66	0.08	0.09	0.03	0.03
7	2.65	2.7	0.095	0.13	0.036	0.048
10	2.68	2.76	0.13	0.13	0.048	0.047

between the individual printed lines forming a single layer. This porosity within FDM-AM is expected to be of about 15% even for 3-D printed samples with 100% material infill which may have an impact at RF when the wavelength is comparable to the air gaps and may cause structural and EM anisotropy [25].

However, the interesting aspect is the freedom in reaching customized mechanical and EM properties, to match specific design requirements. For instance, in [1] the infill factor is modified to control and tailor the properties of 3-D printed dielectrics for lenses design purposes.

The material used for this work is the PLA, a low-cost biodegradable bioplastic with $\varepsilon_r = 2.7$ and $tan\delta = 0.008$, at 1 MHz, but information up to 60 GHz has been provided in literature for a variety of applications [26].

Due to the above-mentioned material property deviation, we first carried out our own EM characterization, by means of the T-resonator technique [27], with two different PLA thicknesses, 0.5 and 2 mm, respectively, to investigate the uniqueness of the dielectric constant values. The T-resonators have been fabricated (see the photos in Fig. 2) and full-wave iteratively simulated for varying relative dielectric constant and conductivity, with the goal of broadband matching the S-parameter measurements.

The microstrip metallization, consisting of a quarter-wavelength open stub connected to a 50-Ω microstrip line, has been manually cut from a 35-μm-thick adhesive copper. The prototypes' photos are shown in Fig. 2. The stub length is L_{stub} = 31 mm resulting in a first resonance at 1.5 GHz, according to the closed form expression:

$$L_{stub} = \frac{n \cdot c}{4 \cdot f_n \cdot \sqrt{\varepsilon_{eff}}}, \qquad (1)$$

where, $n = 1$ is the resonance order, $c = 3 \cdot 10^8$ m/s is the speed of light, $f_n = 1.5$ GHz is the first resonance frequency, $\varepsilon_{eff} = 2.6$ is the first guess (neglecting losses) of the PLA dielectric effective permittivity [1].
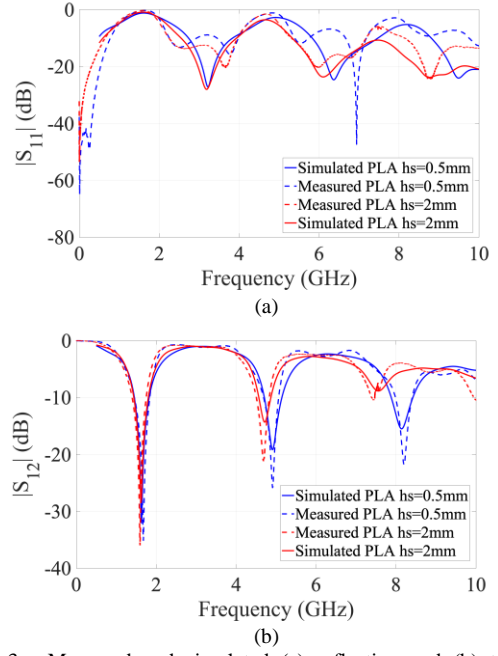

(a)

(b)

Fig. 3. Measured and simulated (a) reflection and (b) transmission coefficient magnitudes of the T-resonators of Fig. 2 on 2-mm-thick (red curves) and 0.5-mm-thick PLA (blue curves).

The Keysight N9952A FieldFox vector network analyzer (VNA) has been used for measuring the S-parameters of the two resonators. The characterization procedure results are reported in Figs. 3(a) and (b), for the samples of Figs. 2.

Table I reports the resulting dielectric properties derived for several frequencies: they are almost independent from the thickness, as confirmed in [26]. However, they show the dispersive behavior of the 3-D printed PLA, and the loss tangent is excessive for exploiting PLA for high performance RF circuits design.

To overcome this drawback, in [28] air cavities of simple geometries have been 3-D etched, resulting in an inhomogeneous material with a reduced effective complex dielectric constant, thus with reduced intrinsic losses. Moreover, in [28] the substrate under the antenna has been almost totally removed resulting in a quasi-air-filled solution below the patch metallization. This led to an increased antenna gain and radiation efficiency, but to weaker mechanical stability when subject to stretching or external pressures, which may also affect the EM performance, including frequency shifting in an unpredictable way.

For this reason, the design freedom of the AM material must be determined by simultaneously accounting for the resulting EM and mechanical properties. One example is reported in [14] where, inspired by recent aerospace and automotive manufacturing, a sandwich-like structure has been investigated for the antenna substrate design. It consists of an etched central core covered by top and bottom thin sheets. The central core is etched using patterns like honeycomb, truss or gyroid, that generate an air-material mixture able to realize a lightweight structure, with a high empty/fill ratio, still robust with respect to flexural and transverse shear. A similar structure is used for the present work and is reported in Fig. 4.
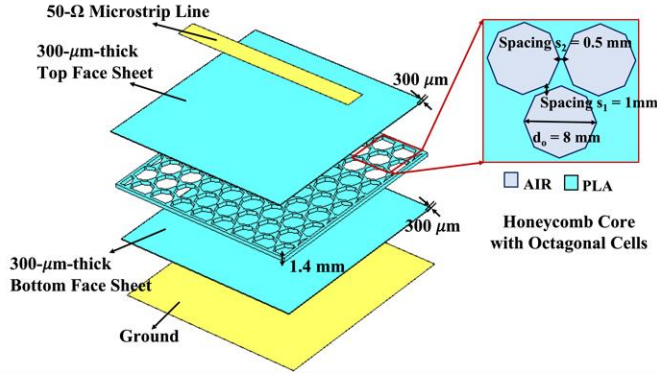
Fig. 4. Exploded view of a microstrip transmission line realized on a PLA substrate engineered as a sandwich-like structure with a honeycomb core with octagonal cells.

Two 300-µm-thick PLA layers are the top and bottom sheets encapsulating a 1.4-mm-thick central core engineered as a honeycomb pattern with octagonal air-filled cells.

The octagonal shape and size, as well as the spacing between adjacent octagons, have been optimized for the best compromise between mechanical robustness and high EM (radiation) performance.

For the present operating frequency, 4-mm-radius octagonal cells have been selected as the best pattern satisfying the two-fold goal of minimizing the amount of PLA, and thus the intrinsic propagating losses, and maintaining a stiff and robust PLA structure. This optimized pattern consists of octagonal air cavities connected by PLA inclusions, with air and PLA percentage of 52% and 48%, respectively. This mixture of air-PLA must be represented using effective EM parameters that account for the field propagating in both materials and the associated boundary conditions due to the material pattern.

Thus, the starting point values of the etched material in Table I have been considered, and the homogenization theory of the Maxwell-Garnett (M.G.) model [29], developed for dielectric mixtures, has been adopted to derive the effective quantities.

From [29], the constituent media and their volume fractions are used to predict an effective dielectric permittivity as follows:

$$\varepsilon_{eff} = \varepsilon_h + 3\, V_i\, \varepsilon_h \left(\frac{\varepsilon_i - \varepsilon_h}{\varepsilon_i + \varepsilon_h - 2\, V_i\, (\varepsilon_i - \varepsilon_h)} \right), \qquad (2)$$

where ε_h and ε_i are the host and inclusion dielectric permittivities (with reference to Table I: $\varepsilon_i = \varepsilon'$, $\varepsilon_h = 1$), respectively, and V_i is the inclusions' volume fraction. Obviously, when V_i tends to 0%, $\varepsilon_{eff} \simeq \varepsilon_h$, and when V_i tends to 100%, $\varepsilon_{eff} \simeq \varepsilon_i$.

The higher the operating frequency, the higher the accuracy required in selecting the PLA inclusions' dimensions, which may cause anisotropy. For this reason, the approximate model of ε_{eff} retrieved through (2) is valid only in the long-wavelength limit, where the static and quasi-static conditions are satisfied. Thus, inclusions' size lower than the smallest wavelength must be selected: as a rule of thumb, it must not exceed one tenth of the wavelength in the effective medium. In this way, (2) may offer a useful initial guess of the effective dielectric constant of
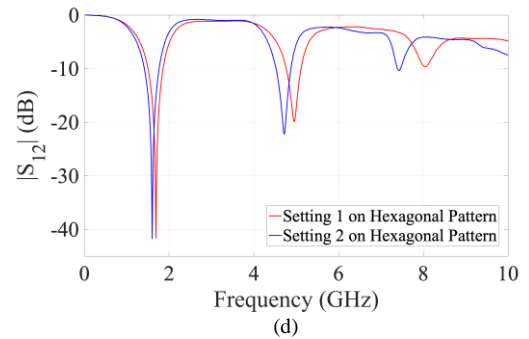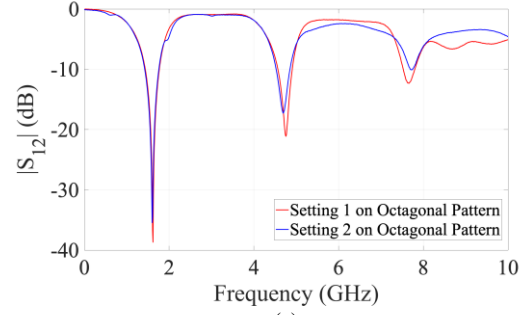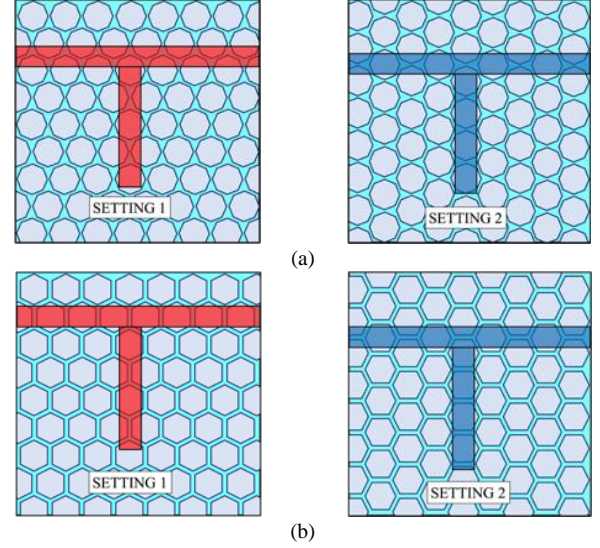

Fig. 5. Resonator's layout positioning on top of the core with (a) octagonal and (b) hexagonal cells patterns; magnitude of the measured transmission coefficients with (c) octagonal and (d) hexagonal cells patterns.

the medium with inclusions; indeed, from (2) an equivalent effective medium with $\varepsilon_{eff} = 1.62$ is derived for an average spacing $[(s_1 + s_2) / 2] = 0.75$ mm (see Fig. 4) among adjacent octagons. This has been obtained by using the PLA relative dielectric permittivity $\varepsilon_i = 2.65$ evaluated at the nominal frequency of 2.45 GHz as shown in Table I, and $\varepsilon_h = 1$, dielectric permittivity of the air.

This result has been validated by full-wave-simulations of the reference T-resonators, with the actual inclusions' shapes accounted for, resulting in a complex effective permittivity with $\varepsilon_{eff}' = 1.8$ and $\varepsilon_{eff}'' = 0.035$ at the nominal frequency of 2.45 GHz. ε_{eff}' is in good agreement with the value computed by (2).

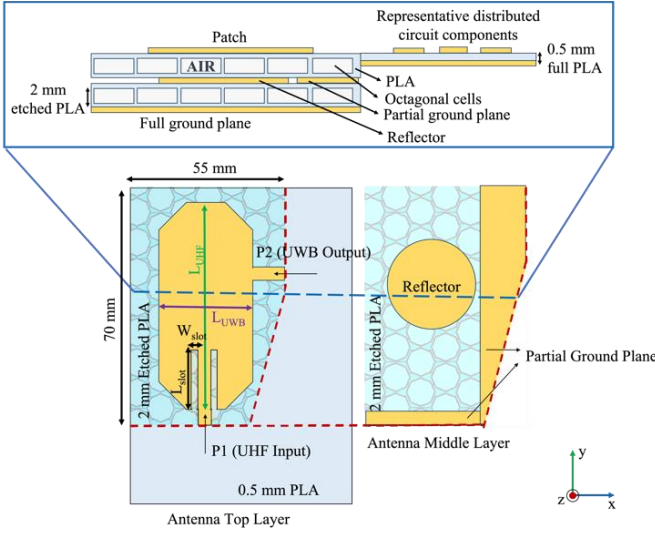It is noteworthy that patterning octagonal cells [14], instead

Fig. 6. Dual-port antenna layout: (top) cross-section, showing the multilayer structure, and (bottom) front views of the top and middle layers.

of the more common hexagonal ones, has the significant advantage of better mimicking an effective homogeneous medium. As representative validations of this concept, Figs. 5(a) and (b) show two different positioning of the same T-resonator on top of the two honeycomb patterns, with octagonal and hexagonal cells, respectively (having the same empty/full ratio, hence the same ε_{eff}). Figs. 5(c) and (d), report the corresponding measured transmission coefficients: when octagonal cells are adopted, the T-resonator frequency behavior is almost unaffected by the different positions, whereas resonance shifts are observed for the hexagonal case, especially at higher frequencies. Similar results have been obtained for other orientations of the microstrip lines, confirming the superior "effective" uniformity of the octagonal pattern.

III. CIRCUIT-LEVEL EM NONLINEAR CO-DESIGN OF THE UHF-UWB TAG

A. Dual-Port Antenna Design

The above described 3-D printed PLA sandwich structure is adopted as the substrate for the design of the antenna, shown in Fig. 6, with two ports: the input port (P1), placed in the lower edge of the antenna, is vertically-oriented, for the reception of the multi-sine excitation at UHF; the output port (P2) is horizontally-oriented, for the backscattering of the passively generated quasi-UWB pulse, and lies on the right-hand side of the antenna. Locations and orientations of P1 and P2 have been carefully optimized to ensure UHF-UWB ports decoupling and cross-polarization at the same time. The unified two-port antenna resulted in a relevant foot-print reduction and system performance enhancements with respect to the solution with two antennas proposed in [14].

The dual-port antenna exploits the flexibility of the AM process: it is designed on a multilayer structure composed of two 2-mm-thick engineered PLA layers of dimension 70×55 mm^2 (described in Section II) sandwiched together. As shown in Fig. 6, the bottom-right corner of the antenna substrate is trimmed to host the rectifier circuitry, on a 0.5-mm-full PLA

layer, obtained by prolonging the antenna top-layer.

The multilayer design, illustrated in Fig. 6 (top), has the dual purpose of providing a wideband antenna behavior, when the UWB port is involved, and of making the structure robustly wearable thanks to the bottom ground plane which decouples the antenna from the environment [30]. The top layer hosts the patch metallization characterized by a stretched shape, whose dimensions are starting from an octagonal shape patch antenna, which provides wideband performance.

The vertical length is $L_{UHF} = 52$ mm, a half wavelength in the effective 3-D printed medium, at 2.45 GHz, for the efficient reception of the RF power at UHF; the insets, with length $L_{slot} = 15$ mm and width $W_{slot} = 1.5$ mm, are designed to match the antenna input impedance to the 50-Ω feeding line.

The horizontal, shorter length is $L_{UWB} = 25$ mm, and has been optimized for antenna operation in the UWB band. Wideband performance is augmented by the layer underneath, hosting a 10-mm-radius-circular reflector whose dimensions and position enhance the antenna bandwidth, to cover up to the fourth harmonic of the highest fundamental UHF tone (2.47 GHz), for the backscattering of the quasi-UWB signal through port (P2) [24], as will be described in the following section. Moreover, vertical and horizontal partial ground planes are introduced in the middle layer to keep the feeding lines' widths tight (5 mm). Finally, at the bottom of the second honeycomb layer a full ground plane makes the tag completely wearable since it is decoupled from the further material layers. To enhance the decoupling between P1 and P2, P2 has been moved towards the patch upper edge.

B. Numerical and Experimental Characterization of the Antenna

The designed dual-port antenna has been full-wave simulated using Computer Simulation Technology (CST) Microwave Studio in the frequency range up to 10 GHz and the fabricated prototype on the 3-D printed 2-mm-thick sandwich structures (see Fig. 6), is measured to validate the design.

In Fig. 7(a) and (b) the measured and simulated reflection coefficients at the UHF and UWB antenna ports, respectively, are superimposed. It is noteworthy that the reflection coefficient at the UWB port [see Fig. 7(b)] shows resonance differences in the lower frequency range, which is useless for backscattering purposes and will be filtered out; while at the higher harmonics, exploited for the quasi-UWB pulse, a good agreement is observed. This is also true for the measured and simulated transmission coefficient between the two ports of Fig. 7(c). From these results it can be observed that the prototype resonates at 2.47 GHz (2.45 GHz predicted) and the UWB measured antenna has a bandwidth ($|S_{22}| < -10$ dB) from 4.5 GHz to 10 GHz.

The simulated antenna radiation patterns are reported in Fig. 8: Fig. 8(a) illustrates the polar plot corresponding to the $\varphi = 0°$ azimuthal plane of the UHF antenna, with the main lobe in the broadside direction having a maximum gain $G_{UHF} = 4.76$ dBi, whereas Fig. 8(b) shows the polar patterns in the $\varphi = 90°$ plane of the UWB antenna evaluated at the II, III and IV harmonics, with predicted gains in the maximum radiation directions of
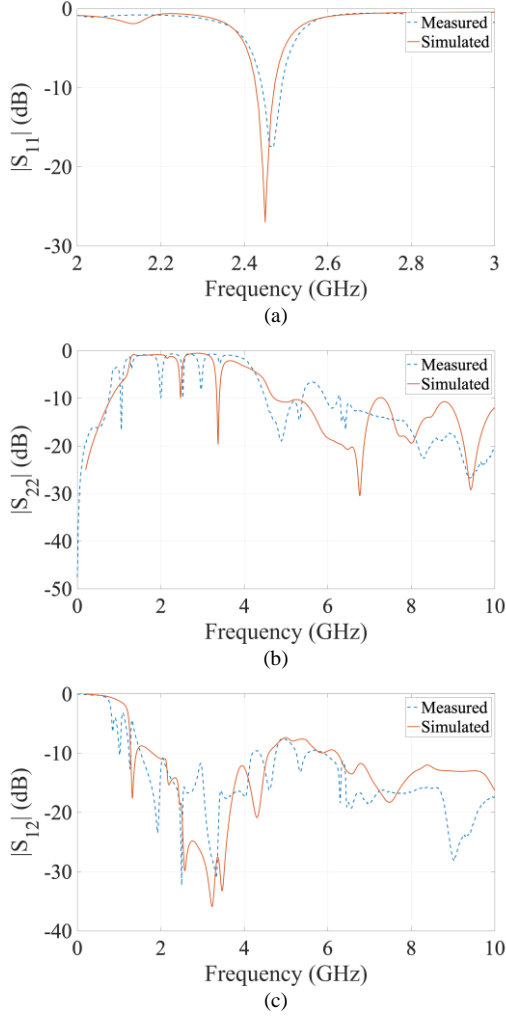
(a)

(b)

(c)

Fig. 7. Reflection coefficient vs frequency at (a) the UHF and (b) the UWB antenna ports; (c) transmission coefficient between the two ports.

(a)

(b)

Fig. 8. Normalized logarithmic polar plots in (a) $\varphi = 0°$ plane at the UHF frequency and (b) $\varphi = 90°$ plane in the UWB band at the II, III and IV harmonics of 2.47 GHz, namely 4.94, 7.41 and 9.88 GHz.

TABLE II
AXIAL RATIO AND E-FIELD COMPONENTS IN THE
MAXIMUM DIRECTION OF RADIATION

Antenna Port	Freq. (GHz)	AR (dB)	E_y (V/m)	E_x (V/m)
UHF	2.47	21.2	8.88	1.23
UWB	2.47	27.6	0.4	6.2
	4.94	39.1	0.11	10.2
	7.41	28.7	0.33	6.78
	9.88	9.6	4.63	7.03

$G_{UWB,II} = 6.24$ dBi, $G_{UWB,III} = 4$ dBi and $G_{UWB,IV} = 8.62$ dBi, respectively.

The designed UHF-UWB cross-polarization is also predicted. Table II reports the electric field vertical and horizontal components, E_y and E_x, respectively, and the axial ratio (AR). By inspecting these values, one can see that at the fundamental UHF frequency the antenna is vertically polarized, and it is horizontally polarized in the UWB band.

C. UHF-UWB Tag Design: Nonlinear Design of a Simultaneous UHF-to-DC and UHF-to-UWB Converter

With the aim of designing a SWIPT tag by the exploitation of a multi-sine excitation, a dual-port nonlinear rectifier has been designed and realized. The two-fold goal of this sub-system is to harvest RF energy from an input multi-sine signal and to convert it into DC with the aim, for instance, to supply a low-power MCU and/or sensor to modulate the passively generated quasi-UWB signal to be exploited for localization purposes.

For efficient nonlinear simulations, the multi-sine excitation has been formulated as in [24], where each tone is represented as the proper hig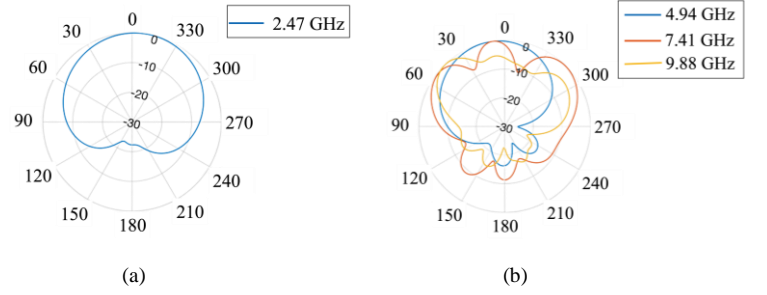her harmonic of the tone spacing frequency, which for the present case is $f_0 = 1$ MHz. Eight tones have been selected around 2.47 GHz, and the excitation can be represented as follows:

$$x(t) = \sum_{i=K_1}^{K_T} x_i \cos(2\pi i f_0 t + \varphi_i), \qquad (3)$$

where x_i and φ_i represent the magnitude and phase of the ith multi-sine excitation, and $K_1 = 2467$ and $K_T = 2474$ are the integers corresponding to the starting and ending higher harmonics of f_0 representing the multi-tone excitations. The center tone at 2.47 GHz, the frequency spacing, and the number of tones have been selected based on the measured antenna resonance and bandwidth.

The circuital schematic of the rectifier and the photo of the top view of the system prototype (including the two-port antenna) are reported in Fig. 9(a) and (b), respectively. The rectifier consists of a single diode (Skyworks SMS7630-079LF) embedded in a linear sub-network composed of: i) a single stub matching network [MN in Fig. 9(b)] at the UHF port rectifier with *SC-Stub*, having length equal to 4.42 mm and width 1.3 mm, *TL-1* having length equal to 11.6 mm and width 1.3 mm and a DC-block capacitance ($C_{MN} = 0.9$ pF); ii) a two-branch output network: the first branch collects the DC output power only, and consists of a low-pass filter loaded by the optimum load ($R_{LOAD} = 790$ Ω), made by a high-quality inductance $L = 1100$ nH [506WLS by American Technical Ceramics (ATC)] and a lumped capacitor ($C_2 = 560$ pF); iii) the second branch drains the higher harmonics to the antenna's UWB port. It consists of a 50-Ω transmission line (*TL-2*, with length: 44.3 mm, width: 1.3 mm), a 50-Ω open-circuit stub (*OC-Stub*,
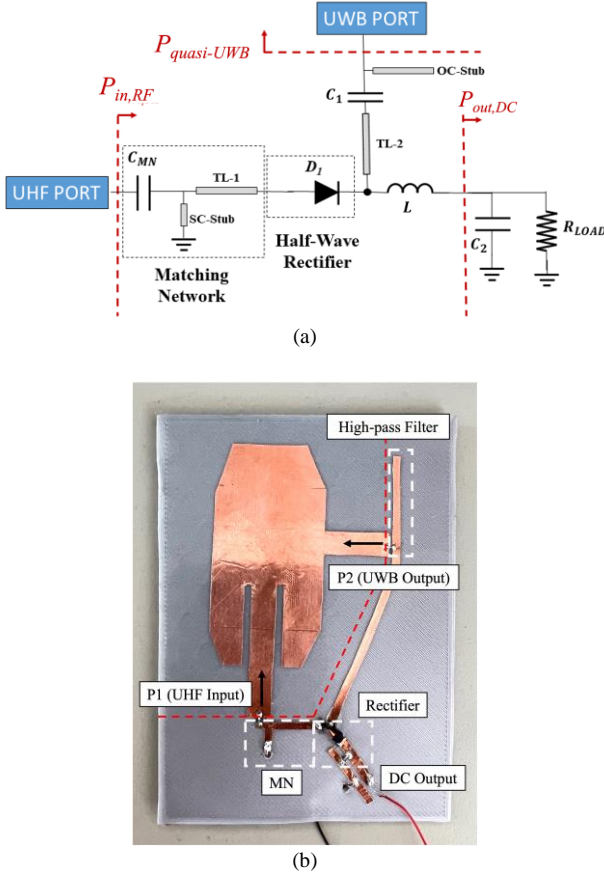
(a)

(b)

Fig. 9. (a) Circuit schematic of the designed dual-mode rectifier; (b) photograph of the system prototype (top view) with the two-port antenna connected to rectifier. UHF and UWB ports are also highlighted.

length: 20.8 mm and width: 1.3 mm) and a capacitor ($C_1 = 0.9$ pF) acting as a DC-block.

All these circuital elements have been used as the design variables inside the nonlinear optimization procedure, with simultaneous specifications on: i) RF-to-DC conversion efficiency; ii) at the UWB port: simultaneous maximization of the power spectral lines near the multi-tone higher harmonics (II, III and IV) and minimization of the near-carrier spectral lines falling in the multi-tone fundamental frequencies; iii) minimization of the return loss at the antenna ports. It is noteworthy that such nonlinear procedure has been carried out in a multi-domain environment [13], combining EM and circuital simulations, in such a way that the dispersive behavior of the antenna is fully accounted for during the nonlinear design process.

Multi-sine excitations, characterized by either constant or parabolic phase distributions, have been considered. In particular, the following formula has been adopted to assign a parabolic phase distribution:

$$\varphi_k = \frac{(k^2-1)\,\pi}{N}, \; k=1, .., N \qquad (4)$$

where N is the number of tones (8 in the present case) and φ_k is the phase of the kth tone.

Nonlinear circuit optimization of the entire rectenna predicts a higher efficiency behavior in the case of parabolic phase
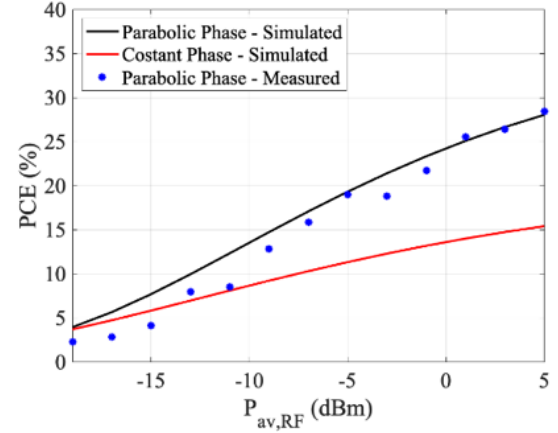

Fig. 10. PCE as a function of the available RF power $P_{av,RF}$ equally distributed over the 8 tones for two different phase distributions: with the tones sharing the same phase (simulated), and with a parabolic phase distribution (simulated and measured).
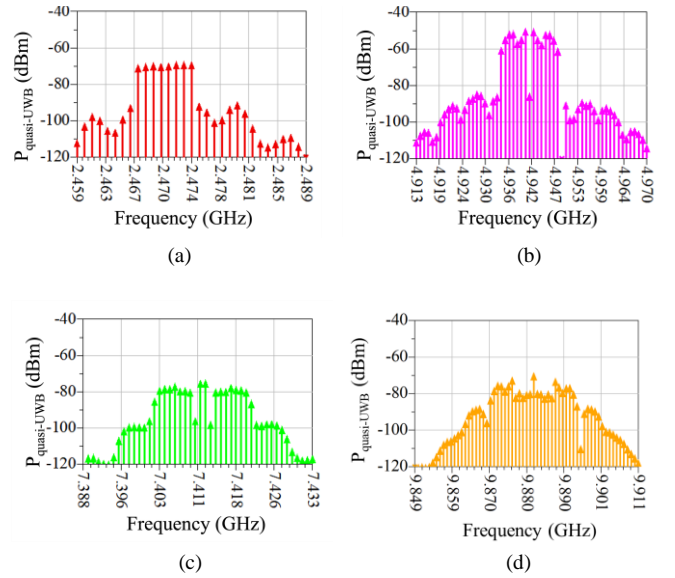

(a)

(b)

(c)

(d)

Fig. 11. Predicted power spectral lines at the antenna UWB port near the (a) first, (b) second, (c) third, and (d) fourth harmonics of the excitation signals, when the total available power is $P_{av,RF} = -15$ dBm.

distribution over the power range of interest (see Fig. 10), which has been chosen for the present design. The two excitations obviously share the same peak-to-average power ratio (PAPR).

The overall rectenna RF-to-DC power conversion efficiency (PCE), is calculated as:

$$PCE \; (\%) = \frac{P_{out,DC}}{P_{av,RF}} \cdot 100, \qquad (5)$$

where $P_{out,DC}$ is the rectified output DC power and $P_{av,RF}$ is the available RF power that may differ from the actual power entering the rectifier ($P_{in,RF}$) which takes into account also the antenna efficiency [31].

The simulations have been performed with the circuit simulation software Keysight Advanced Design System (ADS). The adopted approach is based on a novel formulation of the
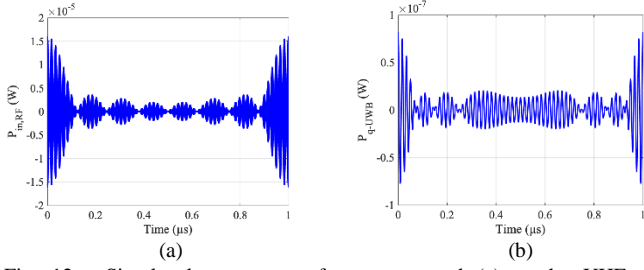
Fig. 12. Simulated power waveforms generated (a) at the UHF port ($P_{av,RF} = -15$ dBm) and (b) at the UWB port.
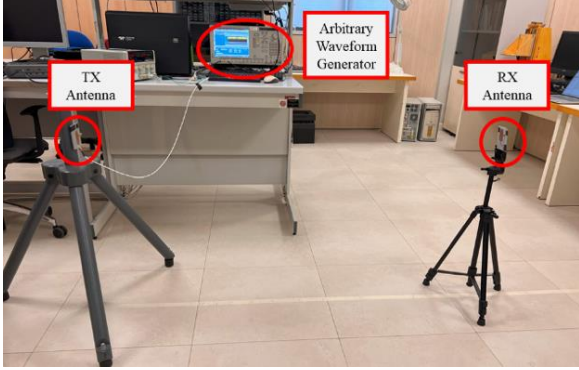

Fig. 13. Measurement setup for energy harvesting validation measurements, showing the transmitting (TX) antenna connected to the arbitrary waveform generator, and the receiving antenna (RX).

harmonic balance (HB) excitation with a high number of tones, that cannot be handled by commercial HB-based simulators. Indeed, each tone is represented as the higher harmonic of the common fundamental frequency (here, $f_0 = 1$ MHz), that is the tone spacing. Thus, the multi-tone simulation is converted into a single-tone one and the efficient optimization of the tones' parameters, such as their number, the frequency spacing, the amplitude, and phase can be easily carried out to satisfy the multi-domain specifications, such as maximization of either the rectified power or voltage and maximization of the higher multi-tone harmonics for the passive generation of the UWB signal. In this way, the spectrum results to be denser (10 thousand of harmonics), but the analysis is faster and more accurate compared to a standard intermodulation analysis [24].

By means of the EM/nonlinear co-design technique, the final UWB effective isotropic radiated power (EIRP) has been computed: for a multi-sine input power of –15 dBm, it results to be below –41.3 dBm/MHz, as requested by the Federal Communication Commission (FCC), considering the maximum UWB antenna gains of 6.24, 4, and 8.62 dBi at the second, third, and fourth harmonics, respectively.

Figs. 11 report the power spectral contents, located near the abovementioned harmonics of interest and exceeding –120 dBm, at the antenna UWB port, to be backscattered from the UWB antenna, when $P_{av,RF} = -15$ dBm. As specified by the nonlinear design, it is worth noticing that the filter at the UWB output minimizes the spectral content near the first harmonic [Fig. 11(a)], which is not part of the quasi-UWB signal to be backscattered. As shown by these plots, the spectral intensities are sufficient for the generation of the quasi-UWB signal but are negligible contributions to be recycled by the harvester. On
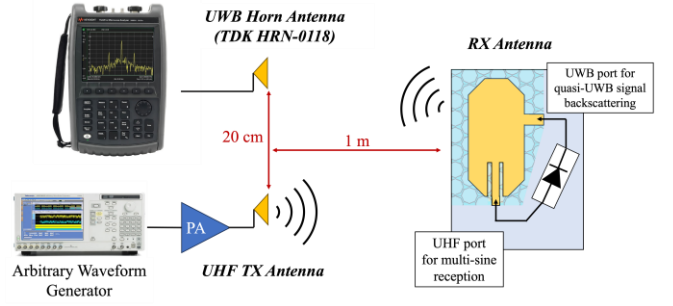

Fig. 14. Schematic view of the setup for measuring the backscattered quasi-UWB signal.

the contrary, the harmonics near the fundamental tones are higher and are reflected from the UWB port to the rectifier by means of the high-pass filter so that they can be further exploited to enhance the PCE. Figs. 12 shows the power waveforms at the input UHF port and at the output UWB port, whose PAPRs are 8.36 and 8.19 dB, respectively. As expected, the output waveform has a slightly different shape with respect to the input one, due to the nonlinearities, and can be exploited as a quasi-UWB signal to be backscattered by the antenna.

IV. UHF-UWB TAG EXPERIMENTAL CHARACTERIZATION

A. UHF-to-DC Energy Power Conversion

In order to validate the simulation results presented in the previous section, a measurements campaign is conducted for what concerns the EH part of the described system. A photo of the measurement set up is reported in Fig. 13 where a complete link is shown: on the transmitter side, the standalone UHF antenna is connected to the arbitrary waveform generator (Tektronix AWG7122C), to radiate the UHF multi-sine excitation; on the receiver side, the two-way rectenna is used and the DC output power is first measured. Fig. 10 shows the measured PCE calculated using (4), superimposed to the simulated ones, with respect to $P_{av,RF}$, ranging from –19 to 5 dBm.

B. UHF-to-Quasi-UWB Signal Generation

A second measurement campaign has been dedicated to the characterization of the quasi-UWB signal generated by the nonlinearities and backscattered from the antenna.

The overall power transmitted from the multi-tone generator is 20.7 dBm, and the gain of the UHF TX antenna is 4.76 dBi: in such conditions $P_{av,RF} = -15$ dBm has been obtained at the UHF port. Indeed, quite low available power has been considered, to ensure that the backscattered signal complies with the FCC UWB mask. Fig. 14 shows the measurement setup, modified from the one of Fig. 13, where a UWB horizontally polarized horn antenna (TDK HRN-0118) is used to capture the quasi-UWB signal backscattered by the two-port rectenna (whose UWB radiation is co-polarized with the horn). The UWB horn is located 20 cm above the antenna transmitting the multi-sine excitation.

Figs. 15 report the measured spectral power lines near the second and third harmonics of the multi-sine excitation, backscattered by the system of Fig. 9, received by the horn, and registered by the Keysight N9952A FieldFox with a resolution
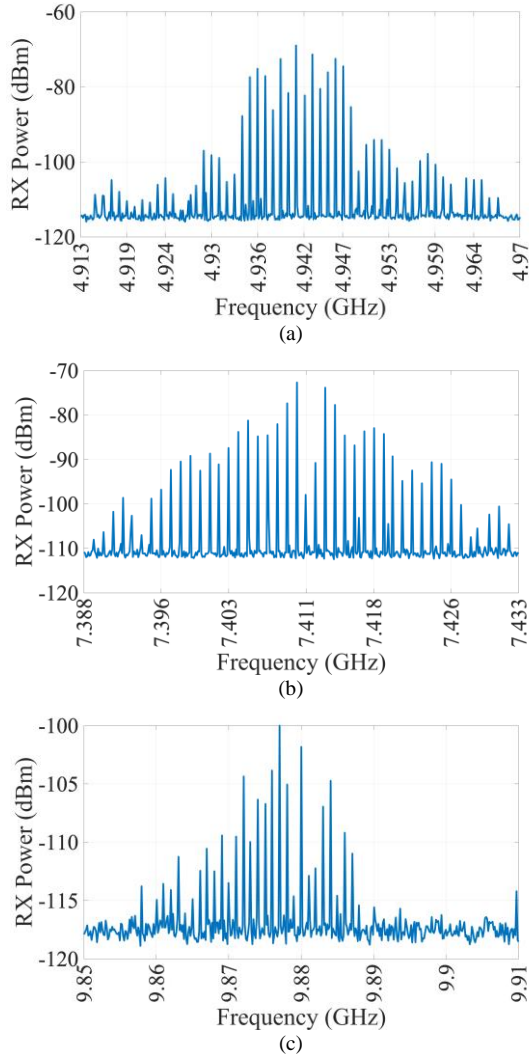
Fig. 15. Measured power spectral lines backscattered by the rectenna and received by the horn associated to the quasi-UWB backscattered signal (total input power $P_{av,RF}$ of –15 dBm), near the (a) second, (b) third, and (c) fourth harmonics.
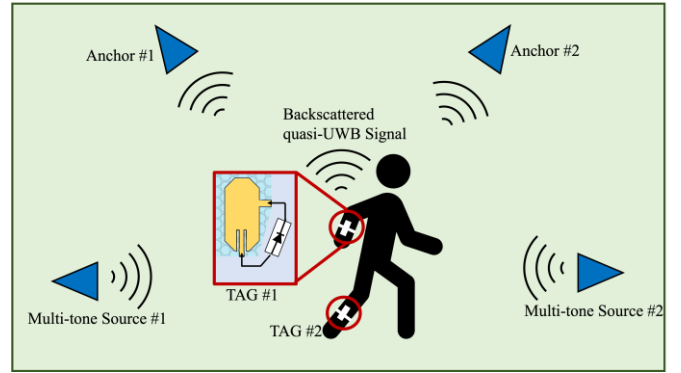

Fig. 16. Envisioned scenario for a practical localization application with single/multiple multi-tone sources and anchor nodes that are placed around an indoor environment for the reception of the backscattered quasi-UWB signals.

commercial single pole double throw (SPDT) switch (i.e., Skyworks SKY59608-711LF) are: supply voltage $V_{BIAS} = 1.8 \div 3.3$ V, supply current $I_S = 5$ µA.

Moreover, the available power levels can satisfy the energy requirements of a low-power commercial MCU, a transceiver operating with LoRa technology, and a three axis accelerometer (400 samples per second) [33]; in particular, if the STM32L476RE MCU and the Semtech SX1280 LoRa transceiver are taken into account, and considering the efficiency of a commercial power management unit (PMU) equal to 50%, it is possible to store sufficient energy to sustain the processing operations of the MCU and a three-axis accelerometer and to transmit all the information about acceleration activities every 160 seconds.

V. CONCLUSIONS

In this work, a fully 3-D printed novel rectenna system on a low-cost PLA substrate has been presented. By connecting a single diode rectifier to a dual-port antenna, a successful integration of EH and UWB backscattering operations has been predicted and validated.

An intensive study of the material characterization has been carried out and a novel etching pattern has been proposed to boost the resulting EM properties of the original material, and thus the EM and circuital performances.

By 3-D printing the PLA with an octagonal pattern, optimized for optimum empty/fill ratio, octagons' dimensions and spacing, it has been demonstrated that high antenna performance can be obtained. A patch-type antenna has been realized on this engineered substrate with two orthogonal excitation ports, designed to achieve both UHF and UWB cross-polarized radiation performance. When the antenna is connected to a rectifier and excited by a multi-tone signal, it can simultaneously harvest RF energy and backscatter a passively generated quasi-UWB signal. The proposed compact solution has been obtained thanks to an accurate and efficient EM/nonlinear co-design strategy that is validated by measurements from both the EH and the backscattering operations point of view.

bandwidth of 3 kHz. The spectral lines near the fourth harmonic resulted to be lower than the minimum useful level exploitable to contribute to the quasi-UWB signal. These measurements are consistent with the predicted transmitted ones of Figs. 11, for both the shapes similarity and the spectral intensities, validating the effectiveness of the EM/nonlinear co-design technique adopted for the present system.

Fig. 16 schematically shows a possible application scenario of this energy autonomous localization system where the signal processing details can be found in [24] and are not reported here for the sake of brevity. The proposed system is suitable for indoor environments where selected anchor nodes can accurately localize it by receiving the backscattered quasi-UWB signal. The harvested DC power is sufficient for modulating the UWB signal and for monitoring the inertial activities of the subject(s) under test by means of an inertial measurement unit (i.e., an accelerometer).

For example, for a $P_{av,RF} = -10$ dBm and $P_{DC} = 12.5$ µW, this power can be used for controlling the dynamic switching and the static bias of the UWB switch [32]. Reference values for a

REFERENCES

[1] T. Whittaker, S. Zhang, A. Powell, C. J. Stevens, J. Y. C. Vardaxoglou, and W. Whittow, "3D Printing Materials and Techniques for Antennas and Metamaterials: A survey of the latest advances," *IEEE Antennas Propag. Mag.*, vol. 65, no. 3, pp. 10-20, Jun. 2023.

[2] D. Masotti, A. Costanzo, M. Del Prete, and V. Rizzoli, "Genetic-based design of a tetra-band high-efficiency radio-frequency energy harvesting system," *IET Microw.*, vol. 7, pp. 1254-1263, Dec. 2013.

[3] V. S. Shilimkar and A. Weisshaar, "Modeling of Metal-Fill Parasitic Capacitance and Application to On-Chip Slow-Wave Structures," *IEEE Trans. Microw. Theory Techn.*, vol. 65, no. 5, pp. 1456-1464, May 2017.

[4] Y. Kim and S. Lim, "Low Loss Substrate-Integrated Waveguide Using 3D-Printed Non-Uniform Honeycomb-Shaped Material," *IEEE Access*, vol. 8, pp. 191090-191099, 2020.

[5] T. Lira-Valdés, E. Rajo-Iglesias, and F. Pizarro, "3-D-Printed Spiral Leaky Wave Antenna With Circular Polarization," *IEEE Open J. Antennas Propag.,* vol. 4, pp. 427-433, 2023.

[6] M. Palandoken, C. Murat, A. Kaya, and B. Zhang, "A Novel 3-D Printed Microwave Probe for ISM Band Ablation Systems of Breast Cancer Treatment Applications," *IEEE Trans. Microw. Theory Techn.*, vol. 70, no. 3, pp. 1943-1953, Mar. 2022.

[7] A. Costanzo and D. Masotti, "Smart Solutions in Smart Spaces: Getting the Most from Far-Field Wireless Power Transfer," *IEEE Microw. Mag.*, vol. 17, no. 5, pp. 30-45, May 2016.

[8] H. Heidari, O. Onireti, R. Das, and M. Imran, "Energy Harvesting and Power Management for IoT Devices in the 5G Era," *IEEE Commun. Mag.*, vol. 59, no. 9, pp. 91-97, Sep. 2021.

[9] Y. Wei et al., "A Multiband, Polarization-Controlled Metasurface Absorber for Electromagnetic Energy Harvesting and Wireless Power Transfer," *IEEE Trans. Microw. Theory Techn*, vol. 70, no. 5, pp. 2861-2871, May 2022.

[10] F. Zafari, A. Gkelias, and K. K. Leung, "A Survey of Indoor Localization Systems and Technologies," *IEEE Commun. Surv. Tutor.*, vol. 21, no. 3, pp. 2568-2599, thirdquarter 2019.

[11] D. Dardari, R. D'Errico, C. Roblin, A. Sibille, and M. Z. Win, "Ultrawide Bandwidth RFID: The Next Generation?," in *Proc. IEEE*, vol. 98, no. 9, pp. 1570-1582, Sep. 2010.

[12] J. Aliasgari, P. Fathi, M. Forouzandeh, and N. Karmakar, "IR-UWB Chipless RFID Reader Based on Frequency Translation Technique for Decoding Frequency-Coded Tags," *IEEE Trans. Instrum. Meas.*, vol. 70, pp. 1-11, 2021, Art no. 8004211.

[13] A. Costanzo, D. Masotti, M. Fantuzzi, and M. Del Prete, "Co-Design Strategies for Energy-Efficient UWB and UHF Wireless Systems," *IEEE Trans. Microw. Theory Techn*, vol. 65, no. 5, pp. 1852-1863, May 2017.

[14] G. Battistini, G. Paolini, A. Costanzo and D. Masotti, "3D-Printable Rectenna for Passive Tag Localization Exploiting Multi-Sine Intermodulation," *2023 IEEE/MTT-S Int. Microw. Symp.*, San Diego, CA, USA, Jul. 2023, pp. 1077-1080.

[15] Q. Zhang et al., "Bioinspired engineering of honeycomb structure–Using nature to inspire human innovation," *Prog. Mater. Sci.,* vol. 74, pp. 332-400, Jul. 2015.

[16] M. Zou, S. Xu, C. Wei, H. Wang, and Z. Liu, "A bionic method for the crashworthiness design of thin-walled structures inspired by bamboo," *Thin-Walled Struct.,* vol. 101, pp. 222-230, Apr. 2016.

[17] L. Li, C. Guo, Y. Chen, and Y. Chen, "Optimization design of lightweight structure inspired by glass sponges (Porifera, Hexacinellida) and its mechanical properties," *Bioinspir. Biomim.*, vol. 15, no. 3, Mar. 2020.

[18] F. E. Sezgin, M. Tanoğlu, O. Ö. Eğilmez, and C. Dönmez, "Mechanical Behavior of Polypropylene-based Honeycomb-Core Composite Sandwich Structures," *J. Reinf. Plast. Compos.*, vol. 29, no. 10, pp. 1569-1579, May 2010.

[19] P. Lu, C. Song and K. M. Huang, "A Two-Port Multipolarization Rectenna With Orthogonal Hybrid Coupler for Simultaneous Wireless Information and Power Transfer (SWIPT)," *IEEE Trans. Antennas Propag.*, vol. 68, no. 10, pp. 6893-6905, Oct. 2020.

[20] S. Shen, C. -Y. Chiu and R. D. Murch, "A Dual-Port Triple-Band L-Probe Microstrip Patch Rectenna for Ambient RF Energy Harvesting," *IEEE Antennas Wirel. Propag. Lett.*, vol. 16, pp. 3071-3074, 2017.

[21] M. Wagih, G. S. Hilton, A. S. Weddell and S. Beeby, "Dual-Polarized Wearable Antenna/Rectenna for Full-Duplex and MIMO Simultaneous Wireless Information and Power Transfer (SWIPT)," *IEEE Open J. Antennas Propag.*, vol. 2, pp. 844-857, 2021.

[22] M. Fantuzzi, D. Masotti and A. Costanzo, "A Novel Integrated UWB–UHF One-Port Antenna for Localization and Energy Harvesting," *IEEE Trans. Antennas Propag.*, vol. 63, no. 9, pp. 3839-3848, Sep. 2015.

[23] A. Boaventura, D. Belo, R. Fernandes, A. Collado, A. Georgiadis, and N. B. Carvalho, "Boosting the Efficiency: Unconventional Waveform Design for Efficient Wireless Power Transfer," *IEEE Microw. Mag.*, vol. 16, no. 3, pp. 87-96, Apr. 2015.

[24] N. Decarli, M. Del Prete, D. Masotti, D. Dardari, and A. Costanzo, "High-Accuracy Localization of Passive Tags with Multisine Excitations," *IEEE Trans. Microw. Theory Techn.*, vol. 66, no. 12, pp. 5894-5908, Dec. 2018.

[25] A. Goulas et al., "The Impact of 3D Printing Process Parameters on the Dielectric Properties of High Permittivity Composites," *Des. J.*, vol. 3, no. 4, p. 50, Nov. 2019.

[26] C.-K. Lee et al., "Evaluation of Microwave Characterization Methods for Additively Manufactured Materials," *Des. J.*, vol. 3, no. 4, p. 47, Sep. 2019.

[27] A. Costanzo, F. Donzelli, D. Masotti, and V. Rizzoli, "Rigorous design of RF multi-resonator power harvesters," in *Proc. 4th EuCAP*, Barcelona, Spain, Apr. 2010, pp. 1-4.

[28] G. Battistini, G. Paolini, D. Masotti, and A. Costanzo, "Wearable Coplanar-Fed 2.45 GHz-Rectenna on a Flexible 3D-Printable Low-Cost Substrate," in *Proc. 52nd Eur. Microw. Conf.*, Milan, Italy, Sep. 2022, pp. 72-75.

[29] A. Sihvola, "Mixing Rules with Complex Dielectric Coefficients," *Subsurf. Sens. Technol. Appl.*, vol. 1, pp. 393–415, Oct. 2000.

[30] L. A. Yimdjo Poffelie, P. J. Soh, S. Yan, and G. A. E. Vandenbosch, "A High-Fidelity All-Textile UWB Antenna With Low Back Radiation for Off-Body WBAN Applications," *IEEE Trans. Antennas Propag.*, vol. 64, no. 2, pp. 757-760, Feb. 2016.

[31] F. Benassi, G. Paolini, D. Masotti, and A. Costanzo, "A Wearable Flexible Energy-Autonomous Filtenna for Ethanol Detection at 2.45 GHz," *IEEE Trans. Microw. Theory Techn.*, vol. 69, no. 9, pp. 4093-4106, Sep. 2021.

[32] A. Costanzo et al., "Energy Autonomous UWB Localization," *IEEE J. Radio Freq. Identif.*, vol. 1, no. 3, pp. 228-244, Sep. 2017.

[33] G. Paolini et al., "RF-Powered Low-Energy Sensor Nodes for Predictive Maintenance in Electromagnetically Harsh Industrial Environments," *Sens.*, vol. 21, no. 2, p. 386, Jan. 2021.

Giulia Battistini (Student Member, IEEE) received the M.Sc. degree in Telecommunications Engineering from the University of Bologna, Bologna, Italy, in 2022. She is currently pursuing the Ph.D. degree in Electronics, Telecommunications, and Information Technologies Engineering. In May 2022, she joined the Department of Electrical, Electronic and Information Engineering "G. Marconi," University of Bologna, as a research fellow within the framework of the PRIN WPT4WID ("Wireless Power Transfer for Wearable and Implantable Devices") project. Her research interests focus on the implementation of 3D printing technologies and materials for the design and fabrication of electronic devices for wearable/implantable wireless power transfer applications.

Giacomo Paolini (Member, IEEE) received the M.Sc. Degree in Biomedical Engineering and the Ph.D. Degree in Electronics, Telecommunications, and Information Technologies Engineering from the University of Bologna, Italy, in 2016 and 2021, respectively. He joined the Interdepartmental Center for Industrial Information and Communication Technologies Research (CIRI ICT) of the University of Bologna as a research fellow within the EU-supported HABITAT (Home Assistance Based on the

Internet of Things for the AuTonomy of everybody) project in 2016. He is currently working as a junior assistant professor at the Department of Electrical, Electronic and Information Engineering "G. Marconi" (DEI) of the University of Bologna. His research interests include microwave radar systems for biomedical applications, indoor positioning exploiting RFID technologies, far-field wireless power transfer (WPT), and simultaneous wireless information and power transfer (SWIPT) systems.

Alessandra Costanzo (Fellow, IEEE) is full Professor at the University of Bologna, Italy since 2018. Her current research activities are dedicated to the design of entire wireless power transmission systems, for several power levels and operating frequencies. She has developed efficient design procedures based on the combination of electromagnetic and nonlinear numerical techniques, adopting both far-field and near-field solutions, thus creating the bridge between system-level and circuit-level analysis techniques of RF/microwave wireless links. She has authored more than 300 scientific publications on peer reviewed international journals and conferences and several chapter books. She owns four international patents. She is past associate editor of the IEEE Transactions on MTT, of the Cambridge International Journal of Microwave and Wireless Technologies and of the Cambridge International Journal of WPT. She is Vice-President for publication of the IEEE CRFID, she has been conference chair of EUMC2022 and of IEEE WiSEE 2023.

Diego Masotti (Senior Member, IEEE) received the Ph.D. degree in electric engineering from the University of Bologna, Italy, in 1997. In 1998 he joined the University of Bologna where he now serves as an Associate Professor of electromagnetic fields. From 2021 he has the role of coordinator of the Telecommunications Engineering Master's Degree course. His research interests are in the areas of nonlinear microwave circuit simulation and design, with emphasis on nonlinear/electromagnetic co-design of integrated radiating subsystems/systems for wireless power transfer and energy harvesting applications. He authored more than 70 scientific publications on peer reviewed international journals and more than 170 scientific publications on proceedings of international conferences. He serves in the Editorial Board of Electronic Letters, of the Hindawi journal of Wireless Power Transfer, of IEEE Access, and is a member of the Paper Review Board of the main Journals of the microwave sector.